William & Mary
CHARTERED 1693

W&M ScholarWorks

VIMS Articles

11-1989

Evaluation Of Automated Threshold Selection Methods For Accurately Sizing Microscopic Fluorescent Cells By Image-Analysis

ME Sieracki
Virginia Institute of Marine Science

SE Reichenbach

KL Webb
Virginia Institute of Marine Science

Follow this and additional works at: https://scholarworks.wm.edu/vimsarticles

 Part of the Environmental Microbiology and Microbial Ecology Commons, and the Marine Biology Commons

Recommended Citation

Sieracki, ME; Reichenbach, SE; and Webb, KL, "Evaluation Of Automated Threshold Selection Methods For Accurately Sizing Microscopic Fluorescent Cells By Image-Analysis" (1989). *VIMS Articles*. 1386.
https://scholarworks.wm.edu/vimsarticles/1386

This Article is brought to you for free and open access by W&M ScholarWorks. It has been accepted for inclusion in VIMS Articles by an authorized administrator of W&M ScholarWorks. For more information, please contact scholarworks@wm.edu.

APPLIED AND ENVIRONMENTAL MICROBIOLOGY, Nov. 1989, p. 2762–2772
0099-2240/89/112762-11$02.00/0
Copyright © 1989, American Society for Microbiology
Vol. 55, No. 11

Evaluation of Automated Threshold Selection Methods for Accurately Sizing Microscopic Fluorescent Cells by Image Analysis†

MICHAEL E. SIERACKI,[1]* STEPHEN E. REICHENBACH,[2] AND KENNETH L. WEBB[1]

College of William and Mary School of Marine Science and Virginia Institute of Marine Science, Gloucester Point, Virginia 23062,[1] and Computer Science Department, College of William and Mary, Williamsburg, Virginia 23185[2]

Received 6 March 1989/Accepted 14 August 1989

The accurate measurement of bacterial and protistan cell biomass is necessary for understanding their population and trophic dynamics in nature. Direct measurement of fluorescently stained cells is often the method of choice. The tedium of making such measurements visually on the large numbers of cells required has prompted the use of automatic image analysis for this purpose. Accurate measurements by image analysis require an accurate, reliable method of segmenting the image, that is, distinguishing the brightly fluorescing cells from a dark background. This is commonly done by visually choosing a threshold intensity value which most closely coincides with the outline of the cells as perceived by the operator. Ideally, an automated method based on the cell image characteristics should be used. Since the optical nature of edges in images of light-emitting, microscopic fluorescent objects is different from that of images generated by transmitted or reflected light, it seemed that automatic segmentation of such images may require special considerations. We tested nine automated threshold selection methods using standard fluorescent microspheres ranging in size and fluorescence intensity and fluorochrome-stained samples of cells from cultures of cyanobacteria, flagellates, and ciliates. The methods included several variations based on the maximum intensity gradient of the sphere profile (first derivative), the minimum in the second derivative of the sphere profile, the minimum of the image histogram, and the midpoint intensity. Our results indicated that thresholds determined visually and by first-derivative methods tended to overestimate the threshold, causing an underestimation of microsphere size. The method based on the minimum of the second derivative of the profile yielded the most accurate area estimates for spheres of different sizes and brightnesses and for four of the five cell types tested. A simple model of the optical properties of fluorescing objects and the video acquisition system is described which explains how the second derivative best approximates the position of the edge.

Epifluorescence microscopy is currently the best method for detecting natural populations of bacteria and protists in aquatic systems and estimating their biomass. Biomass is usually determined by extrapolating linear measurements to estimates of three-dimensional biovolume, which is then converted to biomass units. Linear measurements (e.g., length and width) of individual cells are made visually, either with an ocular micrometer or with a ruler on photomicrographs. Both methods are tedious and time consuming. The introduction of computerized image analysis to this field is automating cell size measurements (3, 23). Image analyzers can easily extract two-dimensional characteristics of cells, such as area and the perimeter array, which can be better used to estimate biovolume. An important ability of these instruments is to provide rapid estimates of the cell size spectra of populations in natural samples. The ability to define the edges of the bright fluorescing cells against a dark background is fundamental to accurately measuring cells.

Segmentation is the process of dividing a digital image into distinct regions by classifying each individual picture element (pixel). Several surveys and textbooks describe methods for segmenting images (2, 8, 17, 22). Thresholding is one of the most popular techniques for segmenting images consisting of an object on a background. A threshold value divides pixels into two groups—those with gray levels greater than or equal to the threshold and those with gray levels less than the threshold. If the threshold is too high or too low, the area measurement of the object will be underestimated or exaggerated, respectively.

If the gray levels of the object and background are not uniform, but probabilistic models for the distributions of the gray levels are known, a Bayes minimum error threshold can be used to locate the best threshold. That is, there is a threshold, t, such that

$$f(x,y) \geq t \Rightarrow P(\text{object} \mid f(x,y) \geq P(\text{background} \mid f(x,y)))$$
$$f(x,y) < t \Rightarrow P(\text{background} \mid f(x,y) > P(\text{object} \mid f(x,y))) \quad (1)$$

where $P(\text{class} \mid f(x,y))$ is the a posteriori probability that the pixel at (x,y) is in the class given the gray level $f(x,y)$. Many researchers assume normally distributed populations with distinct means and standard deviations for the background and object pixels (5, 14). In this case, the image histogram would be the bimodal sum of the two distributions (Fig. 1). Duda and Hart (6) provide a useful reference for statistical decision theory.

This classification approach relies on the statistics of two distinct regions separated by a discontinuity. Sharp edges in a scene may be blurred by the optics or obscured by noise during image acquisition. Further, not all boundaries are step or discontinuous edges. Boundary-placement segmentation techniques attempt to locate the edges of objects even if they are vague or partially obscured. Most of these edge detectors use measures of the gradient or first derivative (13, 16, 21). Huekel (9, 10) suggested an operator that can be generalized to patterns other than step edges.

In previous investigations, epifluorescence microscopy images have been segmented by simple visual thresholding

* Corresponding author.
† Virginia Institute of Marine Science contribution no. 1560.

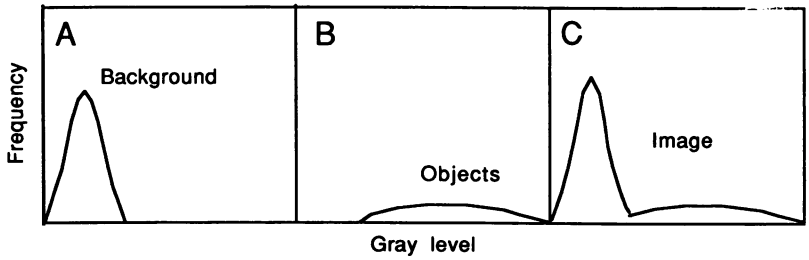

FIG. 1. Histograms of a model image containing normally distributed populations of background (A), object of interest (B), and the whole image (C).

(23) or by computationally intensive methods involving significant preprocessing which were then tested with standard fluorescent microspheres (3). Visual thresholding requires time-consuming human intervention, even if it is performed globally (i.e., one threshold for an entire image). Local thresholds (i.e., separate thresholds for each object) permit more accurate measures but would be prohibitively time consuming. We are troubled by possible measurement bias and inconsistency due to the subjective nature of visual thresholding. There is clearly some variability among separate examinations of a single image by a single human operator as well as among separate examinations of a single image by different operators. Automated thresholding techniques for segmenting microscopic fluorescent objects could relieve the operator of a tedious, time-consuming task and reduce bias and inconsistency. Bjørnsen (3) described such a procedure which uses a number of preprocessing steps which are computationally intensive. This procedure estimated bacterial biovolumes which correlated well with bacterial carbon measurements, but the protocol appeared somewhat ad hoc. The large number of image point operations used in the image averaging and convolutions would be too time consuming to be efficient on small computer systems. We evaluated nine automatic threshold selection methods derived from the image analysis literature for their ability to yield accurate size estimations of standard fluorescent microspheres and fluorescently stained cells representing types commonly found in aquatic plankton samples. The results yielded not only a preferred method of thresholding but also some insights into the optical properties of microfluorescing objects and their detection by video image analysis.

MATERIALS AND METHODS

System hardware. The microscope-image analysis system consisted of a Zeiss Universal microscope, a Hitachi DK-5053 color RGB video microscope camera, a Digital Graphics Systems 1633 image analyzer and a Dual Systems Corp. 83/20 host computer. The microscope is equipped with a 50-W mercury lamp for epifluorescence illumination. The color video camera, equipped with three 17-mm (2/3-in.) CdSe vidicon tubes, detects the image and a camera control unit provides gain controls and manual or automatic black-level and color balance adjustments. Separate red, green, and blue video signals are simultaneously digitized at frame rates (1/30 s) and stored in three image memory planes of the computer. For the analyses described here, only a single image plane (i.e., color) was used. The resolution of the digitizer is 512 × 484 picture elements (pixels) with 8 bits of memory available for each of the three colors. This is equivalent to 256 possible gray levels for each pixel in each color, although in practice the maximum gray level achieved by the system is about 180. The system yields a high-resolution digitized color image on a 48-cm (19-in.) monitor (Ikegami Corp.) which is visually indistinguishable from a direct video image. The image can then be analyzed either by the dedicated 8086 processor with an on-board library of graphics and imaging commands or directly by the 68,000-computer-processing-unit (cpu)-based (8-MHz clock speed) host computer for greater speed. The host computer controls the motorized microscope stage, image and data storage, and trackball interactions for image editing. The system has proved capable of detecting the natural autofluorescence of photosynthetic pigments and commonly used fluorochromes for bacteria and protists (23).

Fluorescent microsphere images. Fluorescently stained latex microspheres (Polysciences, Inc., Warrington, Pa.) of a variety of sizes and dye intensities were used. The intensity set of spheres were all 6.1 μm in diameter (nominal size, ≤3% coefficient of variation) and were stained with 1, 2, 5, 10, 20, and 100% dye concentration. The size set consisted of spheres 0.51, 0.94, and 3.1 μm in diameter (nominal size, ≤3% coefficient of variation) as well as the 6.1-μm spheres and were stained with 100% dye concentration. The spheres have a refractive index (n_D^{20}) of 1.600 and are stained with the fluorochrome coumarin, which has an excitation wavelength maximum of 458 nm and an emission maximum at 540 nm.

Microscope slides were prepared by filtering a diluted portion of the sphere suspension onto a black-stained 0.2-μm-pore-size filter (Nuclepore Corp., Pleasanton, Calif.), placing the filter on a microscope slide, and adding a drop of immersion oil (Resolve, n_D^{23} = 1.515; Stephens Scientific, Kinneton, N.J.) and then a cover slip. Slides prepared this way were used within 2 days since the dye was observed to condense into the center of the spheres after several weeks at room temperature. Images of the spheres were obtained by using the blue excitation filter set of the microscope (Zeiss 487709) consisting of a 450- to 490-nm band-pass excitation filter, a 510-nm dichroic mirror, and a 520-nm long-pass emission filter. For the intensity set of spheres, a 40× oil-immersion objective was used with a 1.25× magnifier. A camera gain of +9 dB gave the best detection over the range of sphere intensities. Black level was manually adjusted to just above the level at which the image started to break up, and color balance was done automatically with a white, transmitted-light image. Images of spheres of each intensity were taken with three and four neutral density (ND) filters (50% transmittance) placed in the emission light path to reduce the sphere brightnesses to approximately that of fluorochrome-stained cells. For the different-size spheres, a 100× Planachromat objective, 2.0× magnifier, no ND

filters, and camera gain settings of 0, +9, and +18 dB for the 3.1-, 0.94-, and 0.51-μm spheres, respectively, were used. Averages of two sequential green image frames were used to improve the signal-to-noise ratio. Subimages of individual spheres were selected from full images for analysis.

Cell cultures. Images of cells from five cultures were tested by the same methods described below. The cultures were (i) the cyanobacteria *Synechococcus* sp. (clone M9, obtained from J. Sieburth), (ii) the cryptophyte *Chroomonas salina* (clone 3C; Culture Collection of Marine Phytoplankton, Bigelow Laboratory for Ocean Sciences, W. Boothbay Harbor, Maine), (iii) an unidentified heterotrophic flagellate (probably a chrysophyte, 4- to 5.5-μm diameter), and (iv) two heterotrophic ciliates isolated from coastal marine waters. Samples from all cultures were fixed with 0.3% glutaraldehyde and stained with proflavine (7) (except for *Synechococcus* sp., for which the autofluorescence of phycoerythrin was used), and slides were prepared by standard methods for epifluorescence microscopy (22). Subimages of 50 to 60 individual cells were obtained with the blue or green (for *Synechococcus* sp., Zeiss 487714) excitation filter set. the 1.25× magnifier, and either a 63× Plan-Neofluar objective (for clone 3C and *Synechococcus* sp.) or a 40× Neofluar oil-immersion objective (for the two ciliates and the heterotrophic flagellate). Camera black-level and color balance were set as above, and the gain was +18 dB. Again, averages of two sequential green (or red for *Synechococcus* sp.) frames were used.

To obtain an independent measure to compare with the automated methods, we visually measured each cell after video image acquisition. We switched to the 100×-objective, increased the magnifier to 2×, and measured the length and width of each cell visually with an ocular micrometer. These measurements were then converted to area by using the formula for either a rectangle with semicircular ends (*Synechococcus* sp.) or an ellipse (flagellates and ciliates).

Profile generation. The profile of a bright spot on a dark background is the brightness value, or intensity, as a function of distance from the center of the spot. Castleman (4) suggested a method for calculating a profile from the image histogram, assuming the object image is circular, concentric, and has a strictly monotonically decreasing intensity away from the center. These are fairly accurate assumptions for images of fluorescent microspheres and many small fluorescing cells. Castleman (4) computes the profile $I(r)$ (intensity as a function of radius) by first calculating the inverse function $R(i)$ (radius as a function of intensity). Because the profile is monotonically decreasing, this inverse function exists. For a digital (discrete) image with a gray scale of 0 to 255, the radius function is:

$$R(i) = \sqrt{\frac{1}{\pi} A(i)} = \sqrt{\frac{1}{\pi} \sum_{j=i}^{255} H(i)} \quad (2)$$

where A is the area of the object brighter than the given intensity i and H is the gray level frequency function or histogram. The profile $I(r)$ is just the inverse of the radius function $R(i)$ computed in equation 2.

For any intensity i, the first derivative of the profile can be calculated as:

$$I'(R(i)) = \frac{(i-1)-(i+1)}{R(i-1)-R(i+1)} = \frac{2}{R(i-1)-R(i+1)} \quad (3)$$

Similarly, the second derivative (used in one of the algorithms described below) is defined as:

$$I''(R(i)) = \frac{I'(R(i-1)) - I'(R(i+1))}{R(i-1)-R(i+1)} \quad (4)$$

For any histogram of a real image, these calculations will probably yield a profile that is somewhat rough. Even a small degree of roughness can interfere with determining the maximum first derivative or other measures. Therefore, we smoothed the profile array with a spatial mean filter with an extent of three samples. That is, successively smoother versions of the profile are calculated by:

$$R_{k+1}(i) = \frac{R_k(i-1) + R_k(i) + (R_k(i+1)}{3} \quad (5)$$

where $R_0(i)$ is defined by equation 2.

The profile was smoothed until all the first- and second-derivative values were smaller in magnitude than the difference between the maximum and minimum gray levels that occur in the image. The sharpest edge possible in a digital image is a change in gray level equal to this difference over a distance of 1 pixel. The result of the discrete calculation of the second derivative should likewise be less than this difference because the magnitude of the first derivative is restricted and the sign of the first derivative of a monotonically decreasing profile changes only at the center of the object.

A smoothed version of the histogram can be calculated from the smoothed profile as done by Wall et al. (25). Given the smoothed profile and the assumption of a concentric, circular, monotonically decreasing gray level object,

$$A_s(i) = \pi R_s(i)^2 \quad (6)$$

and

$$H_s(i) = \begin{cases} A_s(i) - A_s(i-1) & \text{if } i > 0 \\ A_s(0) & \text{if } i = 0 \end{cases} \quad (7)$$

The raw and smoothed profiles and their first and second derivatives are shown in Fig. 2 for an example sphere image.

There are several peaks in the first derivative and corresponding zero-crossings in the second derivative (Fig. 2A and B). To identify a single peak in the first derivative, the array of first derivative values was additionally smoothed (as described above) until there was a single zero-crossing in the second derivative. The resulting very smooth first and second derivatives are shown in Fig. 2C. The effect of these two degrees of smoothing on the image histogram is shown in Fig. 3.

Threshold selection algorithms. (i) Visual (VIS). We visually determined a threshold for each sphere image for the purpose of comparison with other methods and with the known sphere dimensions. Each individual sphere image was displayed alone on the monitor, and thresholds were determined interactively by using the trackball. Moving the trackball increased or decreased the threshold below which the display look-up-table was set to zero. Thresholds were chosen which most closely matched the perceived edges of the sphere. Four determinations were made for each sphere, and the average was used as the visual threshold. Visual thresholds of all sphere images were determined by the same person.

(ii) Middle gray level (MID). MID selects as the threshold the gray level midway between the maximum and minimum gray levels in the image. That is:

$$t = \frac{(I_{max} + I_{min})}{2} \quad (8)$$

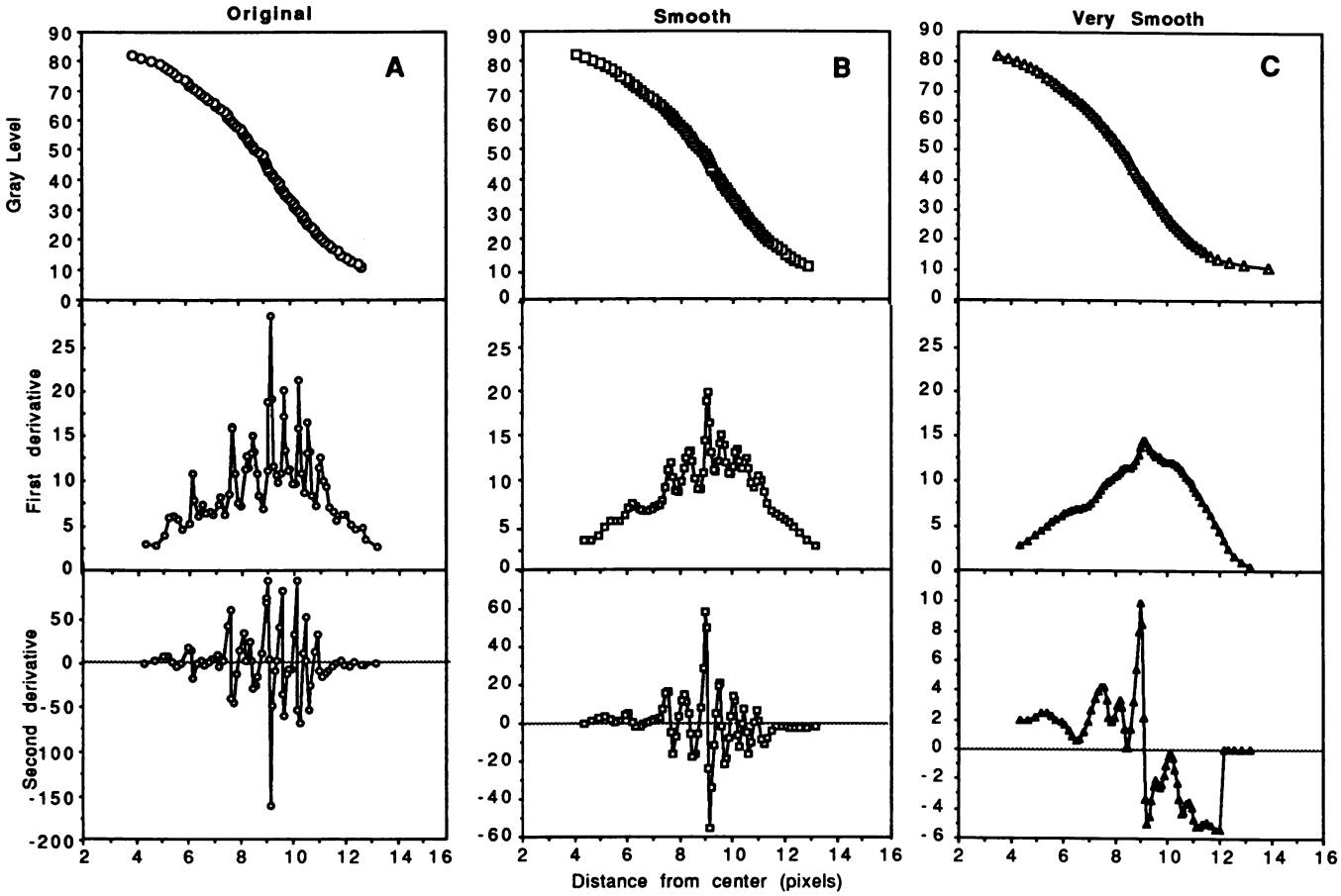

FIG. 2. Effects of smoothing on the histogram-derived profiles and the first and second derivatives for raw (A), smoothed (B), and very smoothed (C) profile data. Data from a single 10% dye intensity sphere with three ND filters.

where I_{max} is the largest gray level in the image and I_{min} is the smallest.

Each segmentation technique assumes an image model. Under the assumptions of the simplest model—a uniform gray level object and background, and a step edge—any algorithm that selects a threshold between the object and background gray levels could be used to segment the image. Clearly, these assumptions do not hold for real images, but MID could provide a good threshold if the assumptions are relaxed a bit. The attractiveness of this method is its simplicity. Imaging systems with histogram boards can perform this type of thresholding at a rate near the standard television frame rate of 1/30 s.

(iii) Minimum of the smoothed histogram (MINSH). Prewitt and Mendelsohn (20) suggested an approach based on the assumption that the pixels in the distinct background and object regions cluster about unequal gray levels (Fig. 1). The modes of the gray levels of the regions appear in the histogram as peaks. The minimum between the peaks is used to divide the distribution. Even if the assumption of distinct regions is relaxed a bit and there exists a small transition between the object and the background, there will be a valley between the histogram peaks.

In real images, the minimum may not be unique, and even if it is, noise and sampling may combine to create false or spurious minima. Smoothing the histogram can alleviate this difficulty (Fig. 3). We implemented MINSH using a decision criterion based on the number of succeeding gray levels with larger distribution counts (before a gray level with a smaller frequency or the image maximum).

Our results indicate that this criterion yields a minimum that corresponds well with a visually selected minimum. For example, the criterion indicated a minimum at 46 for the smoothed histogram shown in Fig. 3C.

(iv) Maximum first derivative (MAXD1). Most edge-based segmentation methods attempt to identify the maximum change in gray level—the gradient or first derivative of the image function. Marr and Hildreth (16) accomplished this by finding the zero-crossings of the second derivative. The first derivative of the smoothed profile can be smoothed until there is a single, second-derivative zero-crossing, corresponding to the maximum first derivative (Fig. 2).

Segmentation methods based on gradient measures are popular, with many variations having been suggested (15). Under the assumption of a circular, concentric, monotonically decreasing spot, some of these variants reduce to finding the maximum first derivative of the profile. Five methods that combine gradient and histogram information are described below.

(v) Minimum of histogram of high-gradient pixels (MINASH). Weszka and Rosenfeld (27) suggested a variant on the search for the minimum of the histogram. They formed a histogram in which only pixels with sufficiently high gradient were counted. The threshold is the minimum of this histogram. In implementing this idea, we included only the 10% of

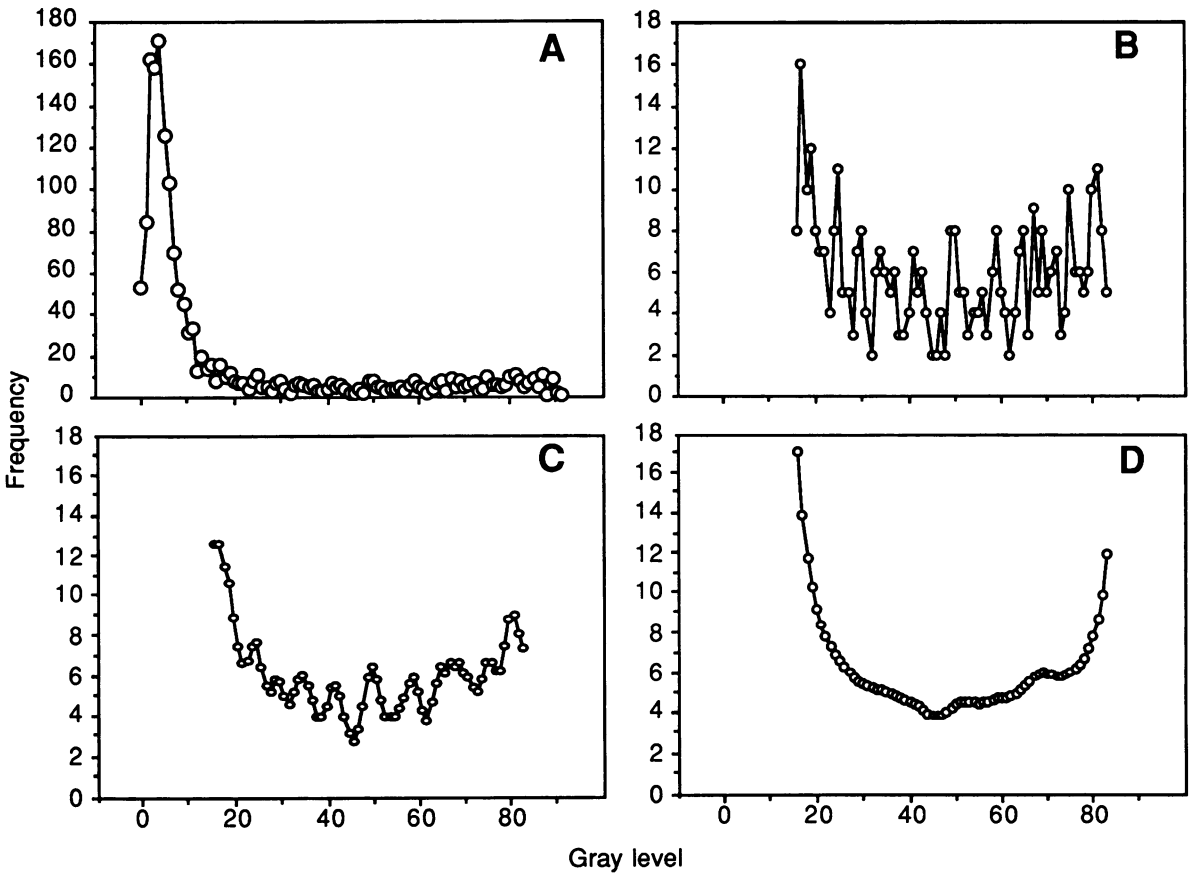

FIG. 3. Effect of smoothing on the image histogram of an example sphere image. The complete, raw histogram is shown in panel A. The region of interest is shown on an expanded scale in the raw (B), smoothed (C), and very smoothed (D) forms. The smoothing method causes artificially high values outside the region of interest. Data are from the example sphere used in Fig. 2.

the pixels with the largest profile gradient. This criterion is also used for MAXASH and AVGASH below.

(vi) Maximum of the histogram of high-gradient pixels (MAXASH). Panda and Rosenfeld (19) proposed a two-pronged approach—finding the minimum of the histogram of low-gradient pixels and the maximum of the histogram of high-gradient pixels. These values are used to divide the two-dimensional histogram of gray level and gradient. For our profiles, segmentation of the low-gradient pixels is not a problem. Moreover, the MINSH/D1 approach (described below) performs an operation similar to this use of low-gradient pixels. Therefore, we examined only the effectiveness of thresholding at the maximum of the histogram of high-gradient pixels.

(vii) Average of the histogram of high-gradient pixels (AVGASH). Katz (12) proposed using the average gray level of the high-gradient pixels.

(viii) Minimum of the quotient of histogram and gradient (MINSH/D1). Weszka and Rosenfeld (28) proposed adding gradient information to the histogram by reducing the relative weight of pixels with high gradients. They reasoned that after discounting edge pixels that tend to fall between the histogram peaks, the minimum of the histogram should be easier to locate. We calculated the ratio of the smoothed histogram frequency to the first derivative of the smoothed profile for each gray level:

$$H_Q(i) = \frac{H_s(i)}{I'(R_s(i))} \tag{9}$$

where the minimum of H_Q is used as the threshold.

(ix) Maximum of the product of histogram and gradient (MAXSH*D1). The last of the five methods that combine gray level and gradient information was proposed by Watanabe (26). This method selects the threshold that maximizes the sum of gradients. Under our assumptions, this is the maximum of the histogram H_p defined as:

$$H_p(i) = H_s(i) \times I'(R_s(i)) \tag{10}$$

(x) Minimum of the second derivative (MIND2). Preliminary observations indicated that the first-derivative or gradient-based methods may underestimate the sizes of spheres. Visual examination of profiles suggested that the proper threshold was closer to the point where the sphere profile begins its rise out of the background noise. At this point, the curvature of the profile is maximum and concave upward. To test this hypothesis, we implemented an algorithm that determined the minimum of the second derivative of the smoothed profile. The use of the second derivative has been suggested by others (16, 18, 22), but to our knowledge its use in this manner is new.

Evaluation of methods. The errors of each method were calculated by subtracting the nominal sphere area from that determined from the threshold selected by each method. The nominal area (in units of pixels) was calculated from the nominal sphere diameter (micrometers) and the pixel-to-micrometer conversion factor of the image analysis system measured at the appropriate magnification. This difference was then expressed as a percentage of the nominal area and

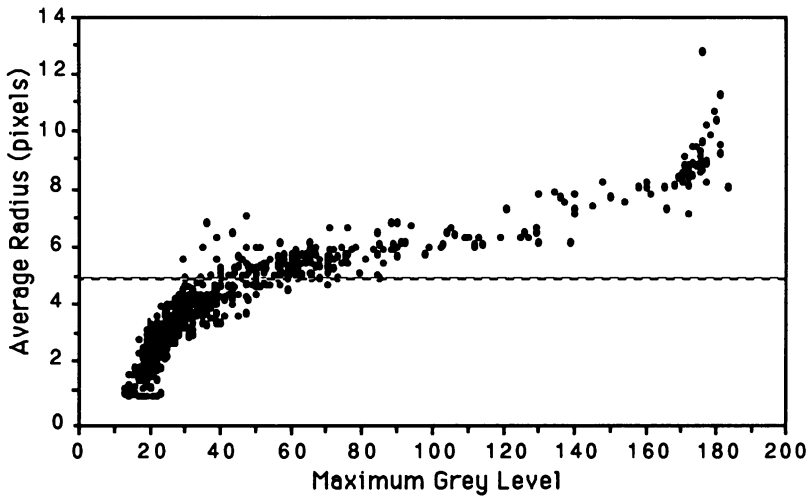

FIG. 4. Size measurements of 6.1-μm-diameter fluorescent microspheres of six different brightnesses (dye intensities of 1, 2, 5, 10, 20, and 100%) with a single threshold gray level of 12, visually chosen to best match the 20% spheres. Horizontal line shows the nominal sphere radius. Fifty spheres of each dye intensity were analyzed.

referred to as the normalized error in area. This was calculated for each sphere measured, and the means and standard deviations were considered in comparing methods. This method retained the sign of the error indicating whether the method over- or underestimated the sphere area. The root mean square error was also calculated for a more absolute measure of the performance of each method unaffected by the sign of the error.

The program which calculates the thresholds from an image histogram by the methods described here is available from us. It was written in C for use on a Unix computer.

RESULTS AND DISCUSSION

Initial attempts to visually determine thresholds for accurate sizing with fluorescent microspheres indicated a complicated relationship between sphere brightness and apparent size (Fig. 4). Sizes of dim spheres were underestimated and those of bright spheres were overestimated. Across an intermediate range of maximum grey levels (about 50 to 170), the relationship was nearly linear. The dimmest spheres were obviously underdetected, and the brightest spheres caused video blooming (11). These results led us to believe that a simple global threshold calibrated to standard fluorescent microspheres is not adequate for accurate sizing. To examine the reasons for this effect, we examined the sphere image profiles.

Preliminary observations of sphere image profiles indicated that the point where the sphere first starts to rise out of the background was most closely associated with the location of the edge as determined by the nominal sphere diameter. This point could be estimated by the minimum of the second derivative of the sphere image profile. Both the visual threshold and the maximum gradient of the profile occurred inside of the actual edge, leading to an underestimate of sphere size. These preliminary observations were generally verified by the performances of the methods on the test sphere images.

Spheres of different brightnesses. The 144 sphere images used for the intensity set are shown in the composite image in Fig. 5. The root mean square errors of the areas for each method (Table 1) indicated that the MIND2 method was generally the most accurate of the automated methods, second only to visual thresholding. MIND2 performed consistently better than the other automated methods for images taken with four ND filters and was the best automated method for three of the six sphere image sets with three ND filters. Thresholds were linearly correlated with average gray level and ranged from 16 to 109 by the visual method (VIS, $r^2 = 0.94$) and from 16 to 137 by MIND2 ($r^2 = 0.87$). The corresponding ranges in sphere image areas were 205 to 469 pixels for VIS and 187 to 550 pixels for MIND2.

The normalized error in area measurement for each of the methods is shown in Fig. 6. The mean and standard deviations illustrate an estimate of accuracy and precision for each thresholding method. This set of pooled data of all the spheres from the intensity set shows that mean errors of the estimates ranged from an underestimation of 39% for MAXASH to an overestimation of 66% for MAXSH*D1. The best method, MIND2, underestimated an average of less than 1%, while visual thresholding resulted in the second lowest normalized error, underestimating by 7%.

The MAXASH method consistently underestimated the sphere size by the largest margin (Fig. 6). This method locates the edge as the maximum of the high-gradient gray levels of the histogram and apparently was weighted by pixels toward the sphere center, leading to a greater underestimation than the other gradient-based methods. The MAXSH*D1 method was most variable and produced the largest overestimates of sphere area (Fig. 6). This method was strongly influenced by the large number of background pixels, causing the estimated threshold value to be too low. It was apparently also strongly influenced by the high-gradient pixels leading to the observed high variability. The other methods generally underestimated sphere size by about the same amount, probably owing to their common dependence on the maximum gradient.

The mean errors of the MAXD1 method were consistently negative across the range of intensities, indicating underestimation of sphere sizes by this method (Fig. 7). In contrast, the MIND2 errors ranged from negative for the dimmer spheres to positive for the brightest spheres. The intensity data in Fig. 7 are presented as the ratio of the maximum measured gray level divided by the visually chosen threshold

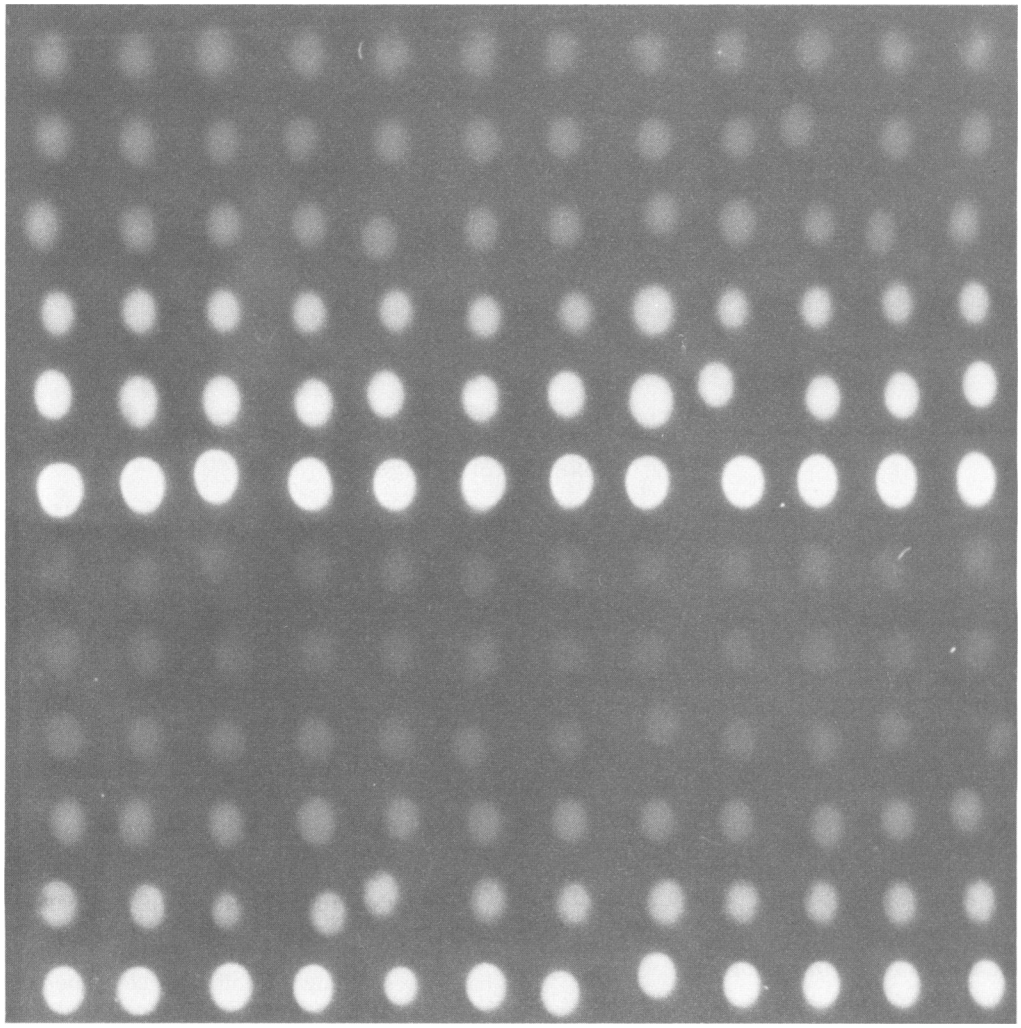

FIG. 5. Digitized images of fluorescent spheres used in this study. This composite image shows the 12 sphere images from each of the six dye intensities (1, 2, 5, 10, 20, and 100%) and illuminated with three (upper six rows) or four (lower six rows) ND filters.

for each sphere to account for the slight differences in background noise levels between the three and four ND filter images (Fig. 5).

Spheres of different sizes. The root mean square errors for the three sphere image sets of different sizes (Table 2) showed a performance pattern similar to that of the intensity sphere set. MIND2 had the lowest error of the automated methods for the 0.94- and 3.1-μm-diameter spheres. The areas of the smallest spheres (0.51 μm) were best estimated by MID, although AVGASH had a low error as well. For the smallest spheres, five of the automated methods had errors lower than or equal to the visual estimates.

The normalized error of the methods for the three sphere image sets of different sizes (Fig. 8) showed a pattern similar to that of the intensity sphere images (Fig. 6). Of the automated methods, MIND2 had the lowest error and MAXSH*D1 had the highest error. There was a general underestimation of sphere size by all methods except MAXSH*D1. VIS significantly overestimated the sizes of the smallest spheres (0.51 μm). MID had less error relative to the other methods with these spheres than with the intensity sphere image set (Fig. 6).

There was no consistent trend of error with sphere size.

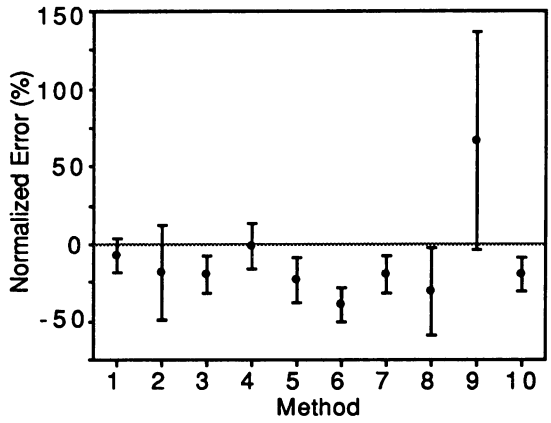

FIG. 6. Normalized error of area measurements for the composite set of intensity spheres. Means and standard deviations are shown (n = 144). Thresholds were selected by the following 10 methods (see text for details): (1) VIS; (2) MINSH; (3) MAXD1; (4) MIND2; (5) MINASH; (6) MAXASH; (7) AVGASH; (8) MINSH/D1; (9) MAXSH*D1; (10) MID.

TABLE 1. Root mean square errors in area (pixels) for the 10 methods of measuring fluorescent microspheres of different intensities (nominal sphere size [6.1-μm diameter] at the magnification used is equivalent to an area of 350 pixels)

% Dye intensity	No. of ND filters	n	Measured avg gray level	Root mean square error of method									
				VIS	MINSH	MAXD1	MIND2	MINASH	MAXASH	AVGASH	MINSH/D1	MAXSH*D1	MID
1	3	12	35.3	25.1	73.6	53.0	66.6	75.2	115.3	53.5	70.9	52.8[a]	69.3
2	3	12	38.0	28.0	85.0	62.2	30.5[a]	75.2	151.2	80.0	77.3	83.4	83.3
5	3	12	43.9	26.4	73.9	62.8	48.0[a]	73.9	138.5	69.1	73.7	67.4	81.6
10	3	12	70.8	37.7	112.3	73.5	79.6	121.0	143.9	75.1	96.9	72.8[a]	91.7
20	3	12	109.4	28.0	106.2	58.5	38.7[a]	89.2	132.5	61.0	101.6	155.4	81.7
100	3	12	163.5	21.6	31.3	35.2	33.0	46.3	62.9	17.5[b]	42.7	399.1	32.9
1	4	12	30.7	42.5	241.0	132.1	44.3[a]	144.0	169.7	125.9	291.2	393.0	82.0
2	4	12	31.0	65.1	114.0	110.0	47.7[b]	114.0	171.6	114.9	311.4	377.7	73.8
5	4	12	35.3	77.4	234.6	105.9	66.2[b]	126.8	165.7	117.0	129.2	451.4	95.1
10	4	12	50.5	59.9	89.7	74.5	44.2[b]	89.7	146.1	78.2	75.8	587.4	78.8
20	4	12	74.4	51.8	76.3	72.4	52.4[a]	76.3	142.9	72.4	76.7	480.4	83.9
100	4	12	136.8	35.3	70.7	70.5	51.9[a]	70.7	144.1	71.8	71.6	306.7	74.6
All	3	72		28.2	84.6	58.7	52.6[a]	83.2	127.5	62.9	79.6	183.9	75.9
All	4	72		57.1	155.4	97.0	51.7[b]	107.0	157.2	99.4	189.4	441.7	81.7
All	3 and 4	144		45.0	125.1	80.2	52.1[a]	95.8	143.1	83.2	145.3	338.4	78.9

[a] Lowest error (excluding VIS).
[b] Error lower than VIS.

Some methods did better with small spheres, such as MIND2, while others, such as MAXASH and MAXSH*D1, did better with larger spheres. The size sphere images were not controlled for brightness, and the 0.94-μm sphere images were not as bright as the others and had higher errors by several of the methods (e.g., MINSH, MAXD1).

Unpaired *t* tests for each sphere type indicated that one-half of the methods resulted in area estimates which significantly departed from the nominal sphere size for all sphere types. Of the remaining five methods (Table 3), MIND2 most often gave estimates not significantly different from the nominal size. Only with the lowest intensity and the 3.1-μm-diameter spheres were the sizes significantly different with this method.

Cell cultures. The methods tested performed in a similar manner with cell images as with the microsphere images, with the exception of the *Synechococcus* sp. cells (Fig. 9). As with the microspheres, MID and the methods combining histogram and gradient information (data not shown) did not perform better than the simpler methods shown in Fig. 9. The *Synechococcus* sp. cells were overestimated by visual thresholding (VIS) as well as by MIND2. MAXD1 performed best for this cell type. This cell type also had the largest variation in percent error of all the cells. These cells were both the smallest and the brightest cells measured, and this may have contributed to this result. The fluorescence of phycoerythrin under green excitation is very bright and appears to have led to very sharp cell edges. Since these cells had the fewest pixels per cell image, their percent error would be expected to be more variable. For the other four cells, MINSH and MAXD1 generally caused an underestimation of cell size, VIS was the best method, and MIND2 was the best automated method. This pattern of method performance was the same as the microsphere results.

Image model. The optical factors leading to the final image of a stained cell or a fluorescing microscopic latex sphere are exceedingly complex. The development of a comprehensive image model would have to account for a large number of

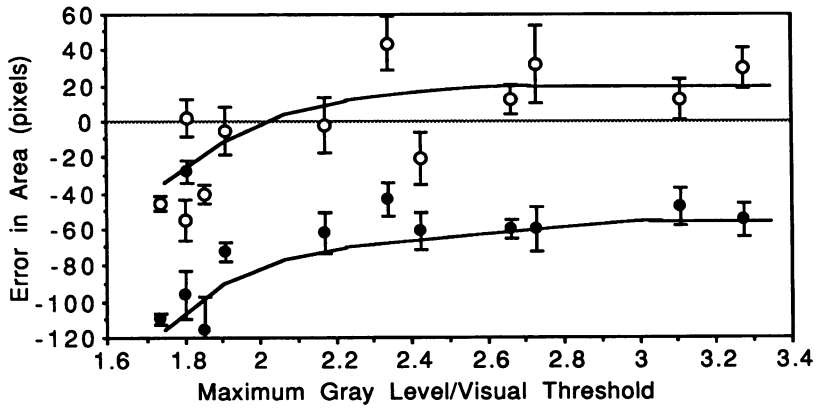

FIG. 7. Mean errors in area across the range of sphere intensities for the MAXD1 (●) and MIND2 (○) threshold selection methods. The abscissa values are the ratio of maximum gray level to visual threshold. Error bars show ±1 standard error. Solid lines show the model results for the two methods for spheres 20 pixels in diameter, a background level of 20, and with a point spread function modeled as a Gaussian distribution with a standard deviation of 1 pixel.

TABLE 2. Root mean square errors in area measurements by the 10 methods with spheres of various sizes (results from the two 100% dye intensity sphere images are included for comparison)

Nominal size		Root mean square error of method									
Diam (μm)	Area (pixels)[a]	VIS	MINSH	MAXD1	MIND2	MINASH	MAXASH	AVGASH	MINSH/D1	MAXSH*D1	MID
0.51	42	18.2	18.3	17.9	12.3	29.9	34.9	8.6	28.5	165.3	7.3
0.94	142	7	59.4	60.7	34.7	71.6	94.3	47.2	66.5	128.4	36.9
6.1[b]	350	21.6	31.3	35.2	33	46.3	62.9	17.5	42.7	399.1	32.9
6.1[c]	350	35.3	70.7	70.5	51.9	70.7	144.1	71.8	71.6	306.7	74.6
3.1	1,539	202.5	309.8	292	191.7	309.8	491.8	302.1	302.8	700.4	274.9

[a] Areas in pixels do not match diameters in micrometers because different magnifications were used for the different-size spheres.
[b] 100% dye intensity spheres with three ND filters.
[c] 100% dye intensity spheres with four ND filters.

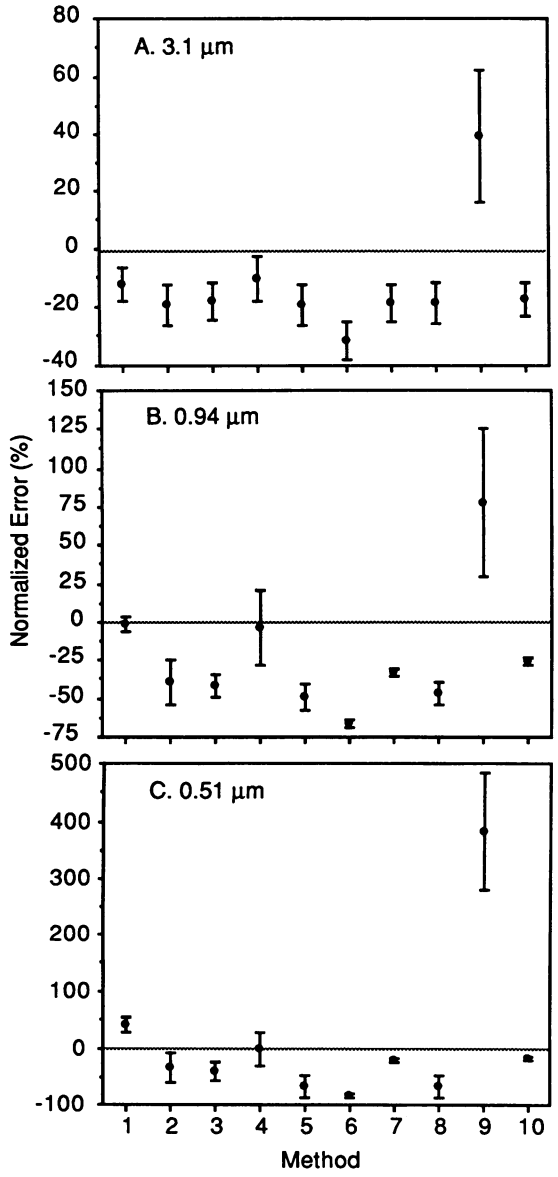

FIG. 8. Normalized error of area measurements for 3.1-μm (A)-, 0.94-μm (B)-, and 0.51-μm (C)-diameter spheres (n = 14). Methods are numbered as described in the legend to Fig. 6. Note different ordinate scales.

parameters which are difficult to measure. The quantum reflection, refraction, and absorbance properties of each optical interface in the system would need to be known for both the excitation and the emitted light. This would include the filters and dichroic mirrors in the excitation and emission light paths in the microscope, objective lenses, glass cover slip, the microsphere surface itself, and the filters and dichroic mirrors in the color camera. As noted by Inoué (11), the modulation transfer functions for many microscope contrast methods have not yet been determined. Knowledge of the quantum yield of fluorescence for the particular dye used in the spheres would be necessary. Then the response of the video tube and associated electronics would need to be modeled. Finally, the response of the analog-to-digital converter and contributions of electronic noise by the system would have to be evaluated. An image model encompassing all these parameters would be outside the scope of this study and does not appear to be necessary to explain our results.

By making some simplifying assumptions, it is possible to develop a model of a fluorescent microsphere image which can account for the better performance of MIND2 over the maximum gradient methods. The refractive index of the latex microspheres is 1.600, and they are mounted in immersion oil with a similar refractive index of 1.515. We may, therefore, assume the sphere itself to be essentially transparent. The sphere contains fluorescing dye molecules which we may assume to be evenly distributed. Considering the small size of these spheres, we may also assume that the excitation light penetrates the sphere to excite all the dye molecules. Since the emission intensity is proportional to the

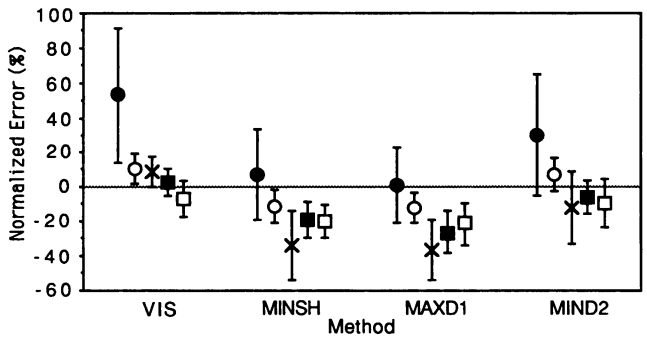

FIG. 9. Normalized errors in area of five different cell cultures for three of the automated methods and visual thresholding. Fifty cells of each of the following cultures were measured: *Synechococcus* sp. (●), *C. salina* (○), a heterotrophic flagellate (×), and two heterotrophic ciliates (□, ■).

TABLE 3. Significance (P) values for unpaired t tests of sphere areas for the different types of spheres and different methods used in this study[a]

Sphere type or % dye intensity	No. of ND filters	P				
		VIS	MINSH	MIND2	AVGASH	MAXSH*D1
Intensity						
1	3	0.06	—[b]	0.01	—	0.99
2	3	—	—	0.16	—	—
5	3	0.01	—	0.02	—	—
10	3	0.39	—	0.18	—	0.12
20	3	0.07	—	0.28	—	0.07
100	3	—	0.68	0.84	0.08	—
1	4	—	0.62	—	—	—
2	4	—	—	—	—	—
5	4	—	0.82	—	—	—
10	4	—	—	0.70	—	—
20	4	—	—	0.90	—	—
100	4	—	—	0.18	—	—
All intensity spheres		—	—	0.50	—	—
Sphere type						
0.51-μm diam		—	—	0.77	—	—
0.94-μm diam		0.32	—	0.63	—	—
3.1-μm diam		—	—	—	—	—

[a] Areas determined by the following methods were significantly different from the nominal sphere sizes for all sphere types: MAXD1, MINASH, MAXASH, MINSH/D1, and MID.
[b] —, $P < 0.01$.

excitation intensity, the brightness profile would be approximated by the equation of a circle.

The edge of an ideal sphere would be defined as the point on the profile with infinite slope, or where the profile approached vertical. This type of perfect edge will never be seen in an optical image processing system owing to the limits of optical resolution, discrete sampling, and the point spread function of the image acquisition (video) system. Instead, the system point spread function would be convolved with the profile, yielding a smoothly inflected curve down to the background intensity level. The maximum gradient would, therefore, be shifted toward the sphere center, yielding an underestimation of sphere size, such as we observed (Fig. 6 and 7). The accuracy of the first versus the second derivative would be determined by the specific point spread function of the image acquisition system. Nonlinearity in the imaging system may be another factor, particularly at low light levels. The combination of the point spread function and the nonlinear response has a different effect on each of the thresholding algorithms. Figure 10 shows the expected results for hypothetical spheres of three intensities for the first- and second-derivative methods. The first-derivative methods will consistently underestimate sphere size, regardless of sphere brightness. In contrast, the second-derivative method will overestimate the size of bright spheres (Fig. 10A) but will underestimate the size of dimmer spheres (Fig. 10C). At some intermediate intensity (Fig. 10B), the second derivative will yield the exact edge position.

We modeled this sphere image using a sphere profile convolved with a Gaussian point spread function. The model inputs are sphere diameter, sphere intensity, and the point spread function (the standard deviation of the Gaussian distribution). The model outputs include the estimated sphere radii from the maxima in the first and second derivatives. From these, the errors in area were calculated to compare with our results. Trials with this model indicated that a Gaussian distribution with a standard deviation of 1 pixel yielded results most like our own. When the intensity values were varied to cover the range of the camera response, the model behaved very similarly to our results (Fig. 7). The MAXD1 method consistently underestimated sphere size, while MIND2 underestimated the size of low-intensity spheres and overestimated the size of high-intensity spheres.

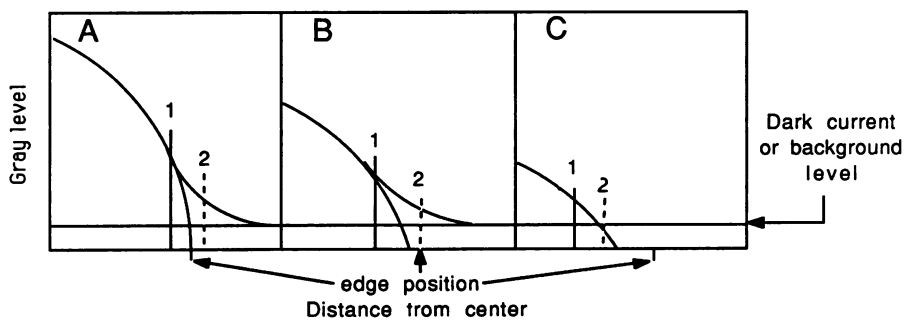

FIG. 10. Model of sphere profiles with high (A), intermediate (B), and low (C) ratios of brightness to background level. The actual sphere edge position is shown along with the positions of (1) the maximum first derivative and (2) the minimum second derivative.

Even with some of the assumptions about the sphere optical properties discussed above relaxed, the sphere edge would still approach vertical and the relative performances of first- and second-derivative methods would be similar to those shown in Fig. 10. This is a different situation from finding edges in an aerial photograph or a microscope image by using transmitted illumination, in which maximum gradient methods generally perform well (20).

Knowing the optical properties of an image acquisition and analysis system, one could correct (to some degree) for nonlinearity and apply a deconvolution filter to each image to attempt to restore it (1). Even when the response and point spread functions are known, this is a very computationally intensive procedure and would not be practical for rapidly processing many images with a relatively small computer system such as ours.

Implementation of automatic thresholding. The MIND2 method took between 30 and 120 s per subimage on our computer system. Because of this, our procedure was to acquire images during the day and process them overnight. Smoothing the histograms and profiles took the most computation time. Faster processors, now inexpensive and widely available, would improve this processing time considerably. For routine use, the second-derivative method can be used to set a threshold for a particular type of cell being measured, for a specific sample, or for each image. Several example cells may be chosen and profiles produced (equation 2). While our profiles were calculated from the equation of a circle, a more appropriate shape could be used, such as an ellipse. The profile would then be smoothed (equation 5), the first derivative calculated (equation 3) and smoothed again, and the threshold calculated by finding the minimum of the second derivative (equation 4). This sequence is relatively easily implemented on a small computer and requires operator intervention only at the point of choosing representative cells. An even more automated method would be to convolve the image with a second-derivative-finding filter (such as a LaPlacian filter) and mapping the result back to the gray level of the image to give the threshold for that image. This method would work best for images containing cells which were similar in intensity and edge characteristics.

For the purpose of obtaining accurate size estimates of fluorescing cells without the subjectivity of visual thresholding, the algorithm based on the second derivative offers the best performance. We believe this application of the second derivative for edge finding is the first such application. Our simple image model provides a framework within which to judge the performance of various sizing methods for fluorescing cells.

ACKNOWLEDGMENTS

This work was funded by ONR grant N00014-84-G-0180.

We thank David Evans for helpful discussions concerning the image model and optics and comments on the manuscript. John Boon provided thoughtful criticism of the manuscript.

LITERATURE CITED

1. **Andrews, H. C., and B. R. Hunt.** 1977. Digital image restoration. Prentice-Hall, Inc., Englewood Cliffs, N.J.
2. **Ballard, D. H., and C. M. Brown.** 1982. Computer vision. Prentice-Hall, Inc., Englewood Cliffs, N.J.
3. **Bjørnsen, P.K.** 1986. Automatic determination of bacterioplankton biomass by image analysis. Appl. Environ. Microbiol. **51**:1199–1204.
4. **Castleman, K. R.** 1979. Digital image processing. Prentice-Hall, Inc., Englewood Cliffs, N.J.
5. **Chow, C. K., and T. Kaneko.** 1972. Automatic detection of the left ventricle from cineangiograms. Comput. Biomed. Res. **5**:388–410.
6. **Duda, R. O., and P. E. Hart.** 1973. Pattern classification and scene analysis. John Wiley & Sons, Inc., New York.
7. **Haas, L. W.** 1982. Improved epifluorescence microscopy for observing planktonic micro-organisms. Ann. Instit. Oceanogr. (Paris) **58**:940–946.
8. **Haralick, R. M., and L. G. Shapiro.** 1985. Image segmentation techniques. Comput. Vision Graphics Image Processing **29**: 100–132.
9. **Hueckel, M. H.** 1971. An operator which locates edges in digitized pictures. J. Assoc. Comput. Mach. **18**:113–125.
10. **Hueckel, M. H.** 1973. A local visual operator which locates edges and lines. J. Assoc. Comput. Mach. **20**:634–637.
11. **Inoué, S.** 1986. Video microscopy, p. 125. Plenum Publishing Corp., New York.
12. **Katz, Y. H.** 1964. Pattern recognition of meteorological satellite cloud photography, p. 173–190. Proceedings of the Third Symposium on Remote Sensing of Environment, 2nd ed. University of Michigan, Ann Arbor.
13. **Kirsch, R. A.** 1971. Computer determination of constituent structure of biological images. Comput. Biomed. Res. **4**:315–328.
14. **Kittler, J., and J. Illingworth.** 1986. Minimum error thresholding. Pattern Recognition **19**:41–47.
15. **Kohler, R.** 1981. A segmentation system based on thresholding. Comput. Graphics Image Processing **15**:319–338.
16. **Marr, D., and E. Hildreth.** 1980. Theory of edge detection. Proc. R. Soc. London Ser. B **207**:187–217.
17. **Mitiche, A., and J. K. Aggarwal.** 1985. Image segmentation by conventional and information-integrating techniques. Image Vision Comput. **3**:50–62.
18. **Nevatia, R.** 1986. Image segmentation, p. 215–231. *In* T. Y. Young and K. S. Fu (ed.), Handbook of Pattern Recognition and Image Processing. Academic Press, Inc., Orlando, Fla.
19. **Panda, D. P., and A. Rosenfeld.** 1978. Image segmentation by pixel classification in (gray level, edge value) space. IEEE Trans. Comput. **C-27**:875–879.
20. **Prewitt, J. M. S., and M. L. Mendelsohn.** 1966. The analysis of cell images. Ann. N.Y. Acad. Sci. **128**:1035–1053.
21. **Roberts, L. G.** 1965. Machine perception of three-dimensional solids, p. 159–197. *In* J. T. Tippett, D. A. Berkowitz, L. C. Clapp, C. J. Koester, and A. Vandenburgh, Jr. (ed.), Optical and electro-optical information processing. MIT Press, Cambridge, Mass.
22. **Rosenfeld, A., and A. C. Kak.** 1982. Digital picture processing, 2nd ed., vol. 2. Academic Press, Inc., Orlando, Fla.
23. **Sieracki, M. E., P. W. Johnson, and J. M. Sieburth.** 1985. Detection, enumeration, and sizing of planktonic bacteria by image-analyzed epifluorescence microscopy. Appl. Environ. Microbiol. **49**:799–810.
24. **Sieracki, M. E., and K. L. Webb.** 1986. A color video image analysis system for studying pico- and nanoplankton populations. EOS Trans. Am. Geophys. Union **66**:1298.
25. **Wall, R. J., A. Klinger, and K. R. Castleman.** 1974. Analysis of image histograms, p. 341–344. Proceedings of the Second International Joint Conference on Pattern Recognition. Copenhagen, Denmark.
26. **Watanabe, S.** 1978. An automated apparatus for cancer prescreening: CYBEST. Comput. Graphics Image Processing **7**: 259–265.
27. **Weszka, J. S., and A. Rosenfeld.** 1974. Threshold selection, 4. Computer Science Center Technical Report Series. TR-336. University of Maryland, College Park.
28. **Weszka, J. S., and A. Rosenfeld.** 1974. Threshold selection techniques, 5. Computer Science Center Technical Report Series. TR-349. University of Maryland, College Park.